Cancer Imaging

RESEARCH Open Access

Preoperative CT-based radiomics to predict the 5-year growth of residual nodules after resection of dominant lung tumors in patients with multiple lung subsolid nodules

Gangze Fu[1], Huajian Chen[2], Enhui Xin[3], Liaoyi Lin[1], Jinjin Liu[1], Lei Chen[3], Guoquan Cao[1], Xiangwu Zheng[1], Yunjun Yang[1*] and Shumei Ma[2*]

Abstract

Background The current prediction of postoperative growth in synchronous nodules remaining after surgical resection of dominant lung tumors in patients with multiple subsolid lung nodules is limited. This study aims to assess the efficacy of preoperative CT-based radiomics in predicting the 5-year growth of these residual nodules (RNs), versus models constructed using commonly utilized CT morphological and quantitative features.

Methods Data from 1392 patients who underwent resection for lung subsolid nodules confirmed as adenocarcinoma or precursor glandular lesions between 2014 and 2018 were retrospectively reviewed. Among the participants, 208 surgical patients with 603 RNs were included, with a follow-up period exceeding five years. Each RN was classified as either grown or stable based on CT imaging. All enrolled RNs were randomly allocated to training and testing sets at an approximately 4:1 ratio. Four models (radiomics, morphological, quantitative, and combined) were built separately by using Random Forest. Model performance was assessed using receiver operating characteristic (ROC) curves, calibration curves, and decision curve analyses, and compared using DeLong test and net reclassification improvement (NRI).

Results Patients harbored 1–26 RNs. 17.9% RNs grew in 5 years. Growth proportions varied by size: 4% for < 5 mm, 8.4% for 5–8 mm, and 48.5% for > 8 mm. Eighteen radiomics features, 5 morphological features, and 2 quantitative features were selected to build the respective models. The radiomics model showed a good ability to predict growth with an accuracy of 97.2% and 86.7% in the training and testing sets, respectively. The radiomics model showed a significantly higher area under the curve (AUC: 0.892) than the morphological model (AUC: 0.834, $P < 0.05$), an advantage over the quantitative model (AUC: 0.862, $P = 0.251$), and similarity to the combined model (AUC: 0.887) in the testing set. The radiomics model showed better reclassification than morphological (NRI = 7.4%; $P = 0.017$) and

*Correspondence:
Yunjun Yang
yyjunjim@163.com
Shumei Ma
shmm2001@126.com

Full list of author information is available at the end of the article

quantitative (NRI = 14%; $P = 0.005$) models in risk stratification. The calibration curves and decision curve analyses further confirmed the clinical value of radiomics.

Conclusions CT-based radiomics demonstrated superior predictive performance for the 5-year growth of RNs, and can be used independently as a promising tool for future clinical guidance.

Keywords Lung, Adenocarcinoma, Radiomics, Multiple subsolid nodules, Computed tomography

Introduction

Lung cancer is the primary contributor of cancer-related mortality [1]. The widespread adoption of low-dose CT for lung cancer screening in recent years has notably increased detection of subsolid nodules [2, 3]. As a result, radiologists and thoracic surgeons are increasingly encountering patients exhibiting multiple lung subsolid nodules [4–6], which are more likely to indicate multicentric lung cancer rather than metastatic cancer [7]. Subsolid nodules include both pure ground-glass nodules (GGNs) and part-solid nodules (PSNs). GGNs or PSNs with a predominant ground-glass component are histopathologically recognized as indicators of lepidic predominant adenocarcinoma [5, 8], formerly known as bronchioloalveolar lung carcinoma [9]. Previous studies [4, 6, 10] have showed that this subtype of lung adenocarcinoma exhibited a probability of being multifocal between 20% and 42%. The presence of synchronous nodules alongside operable dominant lesions poses challenges for radiologists and thoracic surgeons due to the lack of clear management protocols. Decisions regarding intervention and surgery for a dominant lesion must take into account the possibility of growth in other existing nodules [8]. In clinical practice, multiple lung subsolid nodules often cannot be simultaneously resected, leading to the persistence of residual nodules (RNs) [5, 6] after the removal of the dominant tumor.

According to the Lung CT Screening Reporting and Data System (Lung - RADS) version 2022 created by The American College of Radiology (ACR), a slow-growing GGN that meets the criteria of a higher-risk category may be reclassified accordingly. With regard to PSNs showing evidence of growth, biopsy or surgical evaluation is typically the optimal management approach, if feasible [11]. Guidelines usually recommend regular CT monitoring for subsolid nodules over 5 years [8, 12, 13]. Notably, only a small proportion of subsolid nodules show growth after 5 years of stability, and this growth may not always have clinical significance [14–16]. Thus, for patients with multiple lung subsolid nodules, it is imperative to preoperatively predict the 5-year growth of RNs when considering resection of the dominant tumor. Whenever feasible, synchronous nodules deemed at risk should be excised concurrently. Alternatively, postoperative surveillance should also be intensified.

The current ability to predict which of these synchronous nodules may grow during postoperative surveillance is limited. We have previously shown [6] that the growth of RNs was associated with their morphological features. Additionally, other studies [5, 17] have demonstrated that some CT quantitative parameters can predict the growth of RNs. Currently, radiomics serves as a crucial complementary tool capable of extracting high-dimensional data from images, holding increasing significance in cancer research [18]. Radiomics has been previously utilized to predict the benign or malignant nature of subsolid nodules [19, 20]. However, only few studies [21] have utilized radiomics to predict subsolid nodules growth. To our knowledge, it remains unclear whether radiomics can improve clarity in the management and care of patients with multiple lung subsolid nodules. Thus, the aim of this study was to assess the efficacy of preoperative CT-based radiomics to predict the 5-year growth of RNs, compared to models constructed using commonly utilized CT morphological and quantitative features.

Methods

Patients

This retrospective study was approved by our institutional review board, and the requirement for informed consent was waived. We reviewed imaging records from 1392 patients who underwent resection for lung subsolid nodules confirmed as adenocarcinoma (T1N0M0) or precursor glandular lesions (PGL) between January 2014 and December 2018. Among them, patients with RNs manifested as subsolid nodules that remained after resection of the dominant lung tumor were included. Dominant lung tumors were identified as subsolid nodules on preoperative CT imaging that surgical removed, either as the dominant nodule or as the tumor exhibiting the largest solid component or the greatest size among multiple surgically removed subsolid nodules. Surgical patients underwent regular follow-ups at 3-6-month intervals for the first 2 years, and subsequently at 6-12-month intervals thereafter.

The inclusion criteria for patients and RNs were as follows: (1) patients harboring one or more persistent RNs with sizes ranging from 3 to 20 mm and a solid component less than 5 mm on preoperative CT scans; (2) available preoperative non-contrast enhanced CT scans (section thickness ≤ 1.5 mm) [8, 16, 22]; (3) a CT

follow-up period of 5 years or more. The exclusion criteria were as follows: (1) patients with lymph node metastasis identified during surgery; (2) patients with poor-quality preoperative CT images; (2) interval times between the resection of the dominant lung tumor and the preoperative CT scan of 2 months or more. The presence or absence of RNs was identified by a radiologist (reader 1, 2 - year CT diagnosis experience). For uncertain cases, a senior radiologist (reader 2, 10 - year CT diagnosis experience) was consulted to reach a consensus. The measurement of the size (maximum diameter) and solid component of RNs was derived by observers based on preoperative baseline CT scans. A detailed flowchart for the included patients and RNs is shown in Fig. 1. Preoperative CT scans were used as baseline observations for RNs. A total of 603 RNs from 208 patients were therefore included. The initial CT images taken 5 years after resection of the dominant lung tumor served as a reference to assess the 5-year growth of RNs. RNs that remained stable after surgery for 5 years were classified into the non-growth group, while those that exhibited growth either at 5 years or within 5 years of surgery were categorized into the growth group. The following 3 criteria were employed as indicators of RN growth [14, 16]: (1) an increase in size ≥ 2 mm, (2) an increase in the solid component size ≥ 2 mm, and (3) the presence of a new solid component. Subsequently, preoperative CT scans were used for subsequent radiomics, morphologic, and quantitative analysis of RNs. In our study, the decision of whether to perform additional surgery for the growing RNs was reached through a multidisciplinary discussion. This decision - making process comprehensively took into account various factors, including the location and growth rate of the nodules, the patient's psychological state, age, and cardiopulmonary function.

Clinical data including age, gender, smoking history, other past malignancies, initial number of nodules, type of surgery, and resected dominant lung tumor characteristics (location, nodular pattern, lesion size, solid component size and pathology) were recorded. The initial number of nodules was categorized into four subgroups: 2–3, 4–5, 6–7, and ≥ 8. Nodular patterns of the dominant tumor included PSNs and pure GGNs. Lesion sizes of the dominant lung tumor were defined as the

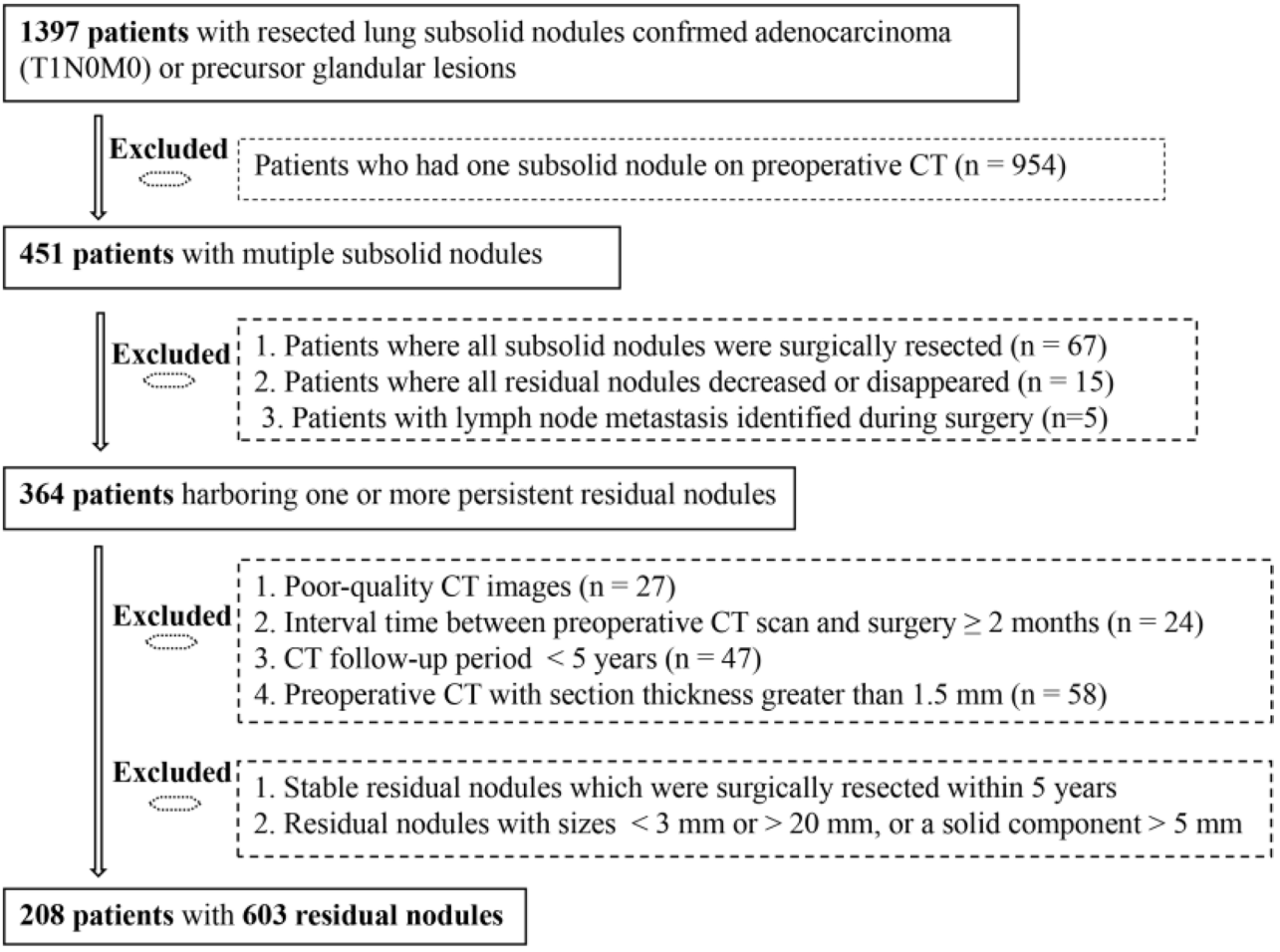

Fig. 1 Study flowchart

average maximal diameter and orthogonal length. Solid component sizes were determined as the largest length of the solid component. Measurements were performed on transverse CT sections. The pathology of the lesion was documented as atypical adenomatous hyperplasia (AAH), adenocarcinoma in situ (AIS), minimally invasive adenocarcinoma (MIA) or invasive adenocarcinoma (IAC).

CT examination

Patients were scanned using the following CT scanners: GE (Discovery CT750 HD, LightSpeed VCT 64, LightSpeed Pro 16), TOSHIBA (Aquilion One 320), or PHILIPS (Brilliance 16) without the use of intravenous contrast. CT scans were performed in the supine position at full inspiration. The parameters used were as follows: tube voltage, 120 kVp; auto mA settings (tube current, 50–150 mA); 0.562–1.375 pitch; 512 × 512 matrix size; reconstruction thicknesses ranging from 0.50 to 1.5 mm using a standard reconstruction algorithm.

Image acquisition and segmentation

The uAI Research Portal (uRP, United Imaging Intelligence Co., Ltd., China) was employed as a platform for image analyses including deep learning-assisted nodule segmentation, manual modification and radiomics analysis [23]. A total of 208 preoperative CT scans were imported into the platform. Firstly, automatic segmentation of RNs was carried out. Subsequently, reader 1 reviewed and modified regions of interests (ROIs) in transverse CT sections layer by layer.

Two weeks later, 50 cases were randomly selected, and the corresponding images were annotated by reader 1 and reader 2 using the same method indicated above for intraclass and interclass consistency analysis. These two readers were blinded to the clinical data and pathological results.

Morphological and quantitative analyses of RNs

RNs were characterized using location, morphological features, and quantitative parameters. Morphological and quantitative parameters of RNs were independently assessed by above two readers. Lung windows on transverse CT images (window width, 1500 HU; window level, -600 HU) were used in this assessment. Discrepancies in interpretation between these two readers were resolved by consensus. To ensure reliability, we performed an interobserver agreement study on a randomly selected subset of 80 lung nodules. Each radiologist independently evaluated these cases for all morphological features. Interobserver agreement was calculated using Cohen's Kappa. For all morphological features, the Kappa values exceeded 0.80, indicating substantial agreement.

The morphological features comprised of size, nodular pattern, lobulated sign, spiculated sign, bubble lucency, vascular sign, well-defined margin, bronchial distortion, pleural attachment, and pleural retraction of RNs. Size was categorized into three subgroups (3–5 mm; 5–8 mm and ≥ 8 mm), and lesion size was defined using the maximal diameter seen on the transverse CT. Nodular patterns included pGGN and PSN. Vascular sign was defined as one or multiple vessels adjacent or through nodules. Pleural attachment was defined as the tumor margin attached to the pleura [24]. Quantitative parameters included three-dimensional (3D) maximum diameter, mean CT value, volume, and mass. Based on the segmented masks of RNs, uRP was used to calculate the 3D maximum diameter, the mean CT value, and the volume. The 3D maximum diameter represented the maximal length of nodules on the 3D image, and the mass was calculated using the Eqs [24, 25]. : $M = V \times [(H_{mean} + 1000) \times 0.001]$, where M is mass in mg, V is volume in mm^3, and H_{mean} is CT value in Hounsfield units (HU).

Radiomics model construction

The radiomics analysis workflow comprised of nodule segmentation, feature extraction and selection, model construction, and model evaluation (Fig. 2). Radiomics features were extracted using the uRP, which was embedded into PyRadiomics, a widely used package. A total of 2264 radiomics features were extracted within the lesion annotation range. Specifically, these features included attributes such as shape ($n = 14$), textures ($n = 72$ per filter, including 21 Gy-level co-occurrence matrix based features, 16 Gy-level run-length matrix based features, 16 Gy-level size zone matrix based features, 14 Gy-level dependence matrix based features and 5 Neighborhood gray-tone difference matrix based features), and first-order statistics ($n = 18$ per filter) from the original and processed images through 24 filters such as wavelet, laplacian and, etc.

Under the premise that each patient could only belong to either the training set or the testing set, all enrolled RNs were randomly allocated to the two sets in an approximate ratio of 4:1, while ensuring that both sets maintained a similar proportion of grown RNs and stable RNs. Feature selection and model construction were performed in the training set. Initially, radiomics features with an ICC value of ≤ 0.80 were excluded. Subsequently, Z-score normalization was applied. Radiomics feature selection was then performed using the least absolute shrinkage and selection operator regression (LASSO) where the number of selected features limited to less than 10% of the sample size to avoid overfitting. The selected features and calculated Radscore were then used for model construction with Random Forest (RF)

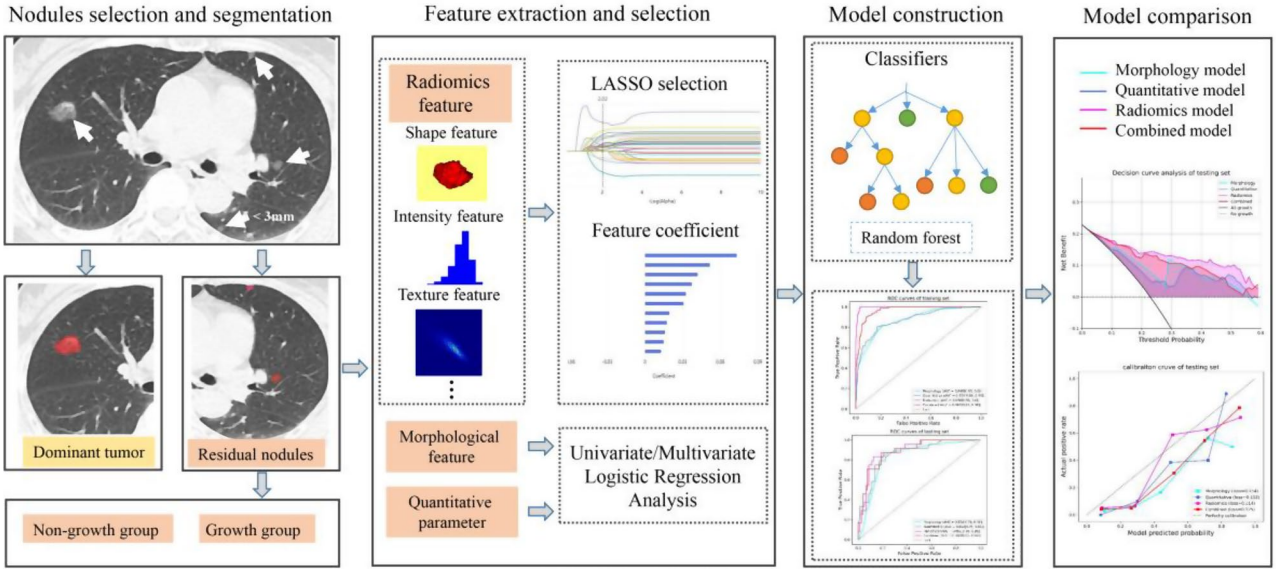

Fig. 2 Radiomics analysis and models construction workflow

algorithm. Hyperparameter optimization was conducted using grid search combined with cross-validation.

Morphological and quantitative model construction

Morphological and quantitative features were selected by univariate ($P<0.1$) and multivariate ($P<0.05$) logistic regression analyses in the training set, respectively. Subsequently, morphological and quantitative models were also developed using RF algorithm. Furthermore, a combined model was constructed by integrating all selected morphological, quantitative, and radiomics features, followed by a two-stage feature selection process using LASSO regression. All models were then built for comparison to the radiomics model.

Model evaluation and comparison

To evaluate the model, we plotted receiver operating characteristic (ROC) curves and calculated performance metrics including the area under the curve (AUC), sensitivity, specificity, and accuracy to quantify the predictive efficacy. The optimal cutoff was derived in training set by maximizing the Youden index. Subsequently, calibration curves were generated to assess the alignment between prediction results and actual outcomes. Brier losses were calculated to measure the difference between predicted probabilities and actual binary results. Decision curve analyses were performed to illustrate the clinical net benefit of the developed models. The DeLong test was employed to compare the AUC values among different models. Additionally, the net reclassification improvement (NRI) was computed to quantify the clinical improvement between the models.

Statistical analysis

Statistical analyses were performed using the Python (version 3.9) and R (version 4.2.1) software. Continuous data that follows a normal distribution are shown as means ± standard deviations (SD), whereas non-normally distributed continuous data are shown as medians (interquartile range). Categorical data are shown as numbers (percentages). For the analysis of continuous variables, independent samples t-tests or Mann-Whitney U tests were utilized, while categorical variables were analyzed using Pearson's chi-squared tests or Fisher's exact tests to discern significant differences between two groups. Characteristics with a $P<0.1$ in the univariate logistic regression analysis were used as input variables for multivariate logistic regression analysis, with the aim of identifying risk factors. DeLong test was used to compare AUC values between two different models, and NRI was calculated to quantify the clinical improvement between models. A p-value <0.05 was considered statistically significant.

Results

Patient characteristics

Patients harbored 1 to 26 RNs. Among the 208 enrolled patients (67 males and 141 females; median age: 60 years, range 36–71 years), 79 (38.0%) exhibited 1 or more grown RNs, while 129 (62.0%) had stable RNs. Clinical characteristics of patients and their dominant tumors are shown in Table 1. Among the 79 patients with growing RNs (Figs. 3 and 4), 20 (25.3%) patients exhibited growth in multiple RNs, including 14 patients with 2 growing RNs (Fig. 4), 4 patients with 3 growing RNs, 1 patient with 4 growing RNs, and 1 patient with 5 growing RNs. Nineteen patients underwent further surgical resection

Table 1 Clinical characteristics of patients

Clinical characteristics	Total (208)	Patients with grown RNs (79)	Patients with stable RNs (129)	*P**
Age	60.0 (53.0-65.3)	63.0 (57.5–68.0)	58.0 (52.0–65.0)	0.043
Female	141 (67.8%)	47 (59.5%)	94 (72.9%)	0.718
History of smoking	37 (17.8%)	18 (22.8%)	19 (14.7%)	0.212
Other past malignancies	27 (13.0%)	11 (13.9%)	16 (12.4%)	0.354
Initial number of nodules				0.002
2–3	99 (47.0%)	31 (39.2%)	68 (52.7%)	
4–5	48 (23.1%)	19 (24.1%)	29 (22.5%)	
6–7	24 (11.5%)	7 (8.9%)	17 (13.2%)	
≥ 8	37 (17.8%)	22 (27.9%)	15 (11.6%)	
Type of surgery				0.050
Wedge resection	39 (18.8%)	16 (20.3%)	23 (17.8%)	
Segmentectomy	43 (20.7%)	15 (19.0%)	28 (21.7%)	
Lobectomy	107 (51.4%)	39 (49.4%)	68 (52.7%)	
Combination	19 (9.1%)	9 (11.4%)	10 (7.8%)	
Location of the dominant tumor				0.692
Left upper lobe	64 (30.8%)	25 (31.7%)	39 (30.2%)	
Left lower lobe	17 (8.2%)	7 (8.9%)	10 (7.8%)	
Right upper lobe	80 (38.5%)	26 (32.9%)	54 (41.9%)	
Right middle lobe	16 (7.7%)	7 (8.9%)	9 (7.0%)	
Right lower lobe	31 (14.9%)	14 (17.7%)	17 (13.2%)	
Features of the dominant tumor				
Lesion size (mm)	17.3 (13.0-22.4)	18.1 (13.8–22.6)	17.1 (12.5–22.2)	0.081
Nodular pattern				0.001
Pure GGN	59 (28.4%)	21 (26.6%)	38 (29.5%)	
PSN	149 (71.6%)	58 (73.4%)	91 (70.5%)	
Pathology				0.014
PGL	38 (18.3%)	13 (16.5%)	25 (19.4%)	
MIA	50 (24.0%)	18 (22.8%)	32 (24.8%)	
IAC	120 (57.7%)	48 (60.8%)	72 (55.8%)	

GGN, pure ground-glass nodule; PSN, part-solid nodule; PGL, precursor glandular lesions; MIA, minimally invasive adenocarcinoma; IAC, invasive adenocarcinoma

for growing RNs (Fig. 3), excluding two patients who underwent a second surgical intervention for PSN with a solid component exceeding 5 mm in the contralateral lung. Two patients developed lymph node metastasis during follow-up due to RN progression without undergoing further surgical treatment (Fig. 4).

Nodule growth patterns and clinical outcomes

Out of the total 603 RNs, 108 (17.9%) were categorized into the growth group, whereas 495 (82.1%) were categorized into the non-growth group. Of the 108 RNs in the growth group (Figs. 3 and 4), 103 (95.4%) increased in size, 37 (34.3%) displayed growth of a solid component, and 5 (4.6%) developed a new solid component. At 2.7 ± 0.8 years of follow-up, 23 grown RNs (21.3%) from 18 patients (22.8%) were surgically removed, of which 2 were AIS, 9 were MIA, and 12 were IAC. The proportion of RNs exhibiting 5-year growth across various size classifications was as follows: 4% for lesions smaller than 5 mm, 8.4% for lesions ranging from 5 to 8 mm, and 48.5% for lesions greater than 8 mm. Additionally, when considering different nodular patterns, the growth proportion was 14.4% for pure GGNs and 74.3% for PSNs.

Morphological and quantitative features of growth and non-growth RNs

The morphological feature assessment demonstrated excellent interobserver reliability, with Cohen's kappa coefficients exceeding 0.80 for all categories, ensuring robust diagnostic consensus. Morphological features and quantitative parameters of RNs in these two groups are summarized in Table 2. There were no significant differences in lesion location, lobulated sign, vascular sign and well-defined margin between the two groups ($P > 0.05$). RNs ≥ 8 mm dominated the growth group (74.1% vs. 17.2% in non-growth, $P < 0.001$), whereas 94.2% of non-growth nodules were ≤ 8 mm. PSNs were strongly associated with growth (24.1% vs. 1.8% in non-growth, $P < 0.001$), while pure GGNs predominated in the non-growth group. Spiculated sign, bronchial distortion, bubble lucency, pleural retraction, pleural attachment were significantly enriched in the growth group. Growth

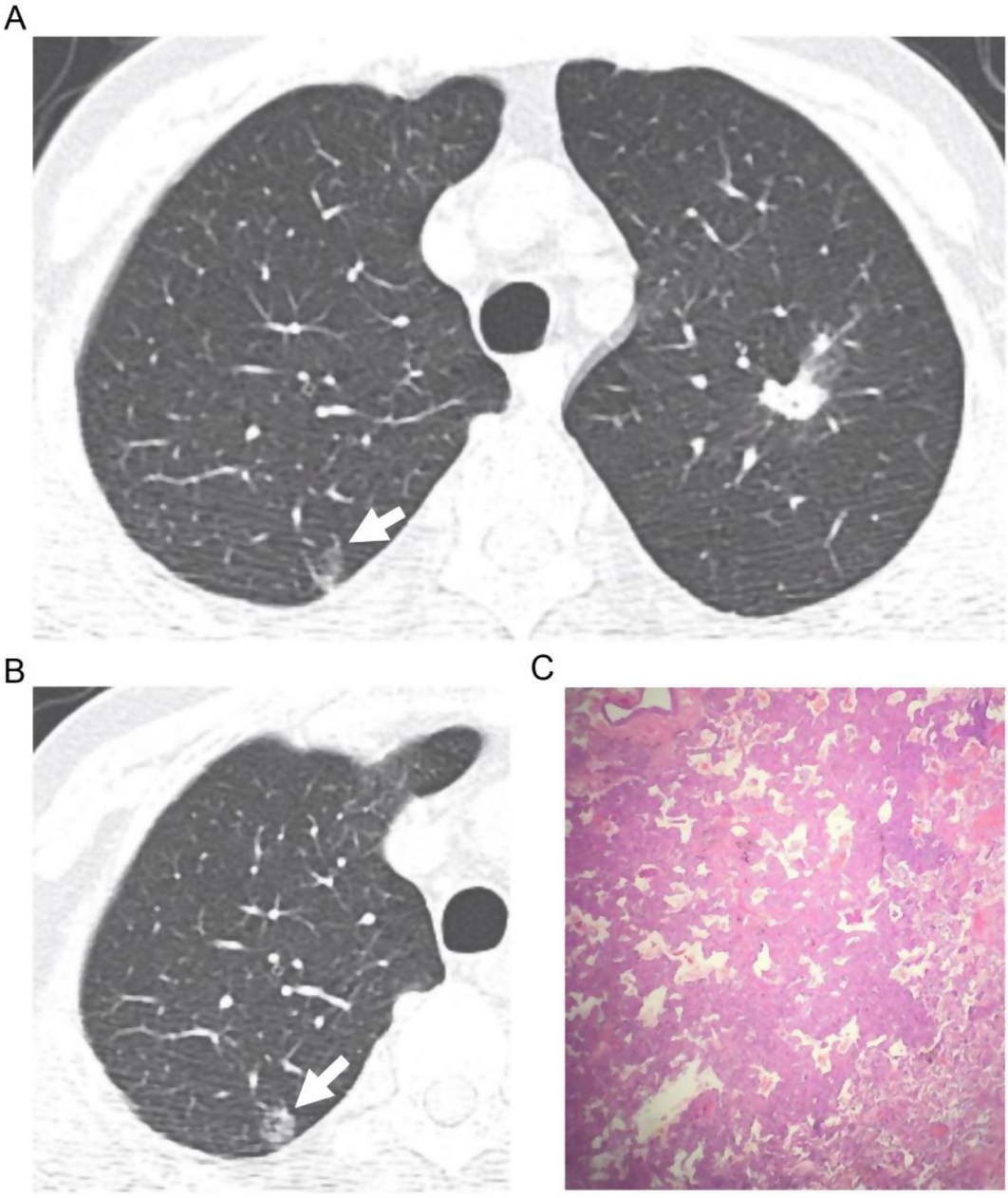

Fig. 3 Case study showing a 64-year-old male with two subsolid nodules. (**A**) The dominant lung tumor manifesting PSN was seen in the left upper lobe. A RN presenting as PSN (arrow) located in the right upper lobe measured 8 mm with a 2 mm solid component. (**B**) After lobectomy of the dominant lung tumor, this RN (arrow) exhibited growth, reaching a size of 10 mm after 2 years of follow-up, where the solid component size also exhibited growth. (**C**) After a segmentectomy, it was confirmed as an IAC with lepidic and acinar patterns (HE, ×100)

RNs demonstrated larger 3D maximum diameter, higher mean CT values, and substantially greater volume and mass ($P < 0.001$).

Feature selection for model construction

A total of 414 stable RNs and 84 growing RNs from 165 patients were included in the training set, and a total of 81 stable RNs and 24 growing RNs from 43 patients were in the testing set. The proportion of growing and stable RNs in the two sets exhibited no significant differences ($P = 0.188$).

After removing features with an ICC ≤ 0.80, 2186 radiomics features were maintained for feature selection. A total of 18 radiomics features [see Additional file 1] were selected using LASSO in the training set for construction of the radiomics model. Additionally, 5 morphological features (size classification, nodular pattern, bronchial distortion, bubble lucency, and pleural attachment) and 2 quantitative parameters (3D maximum

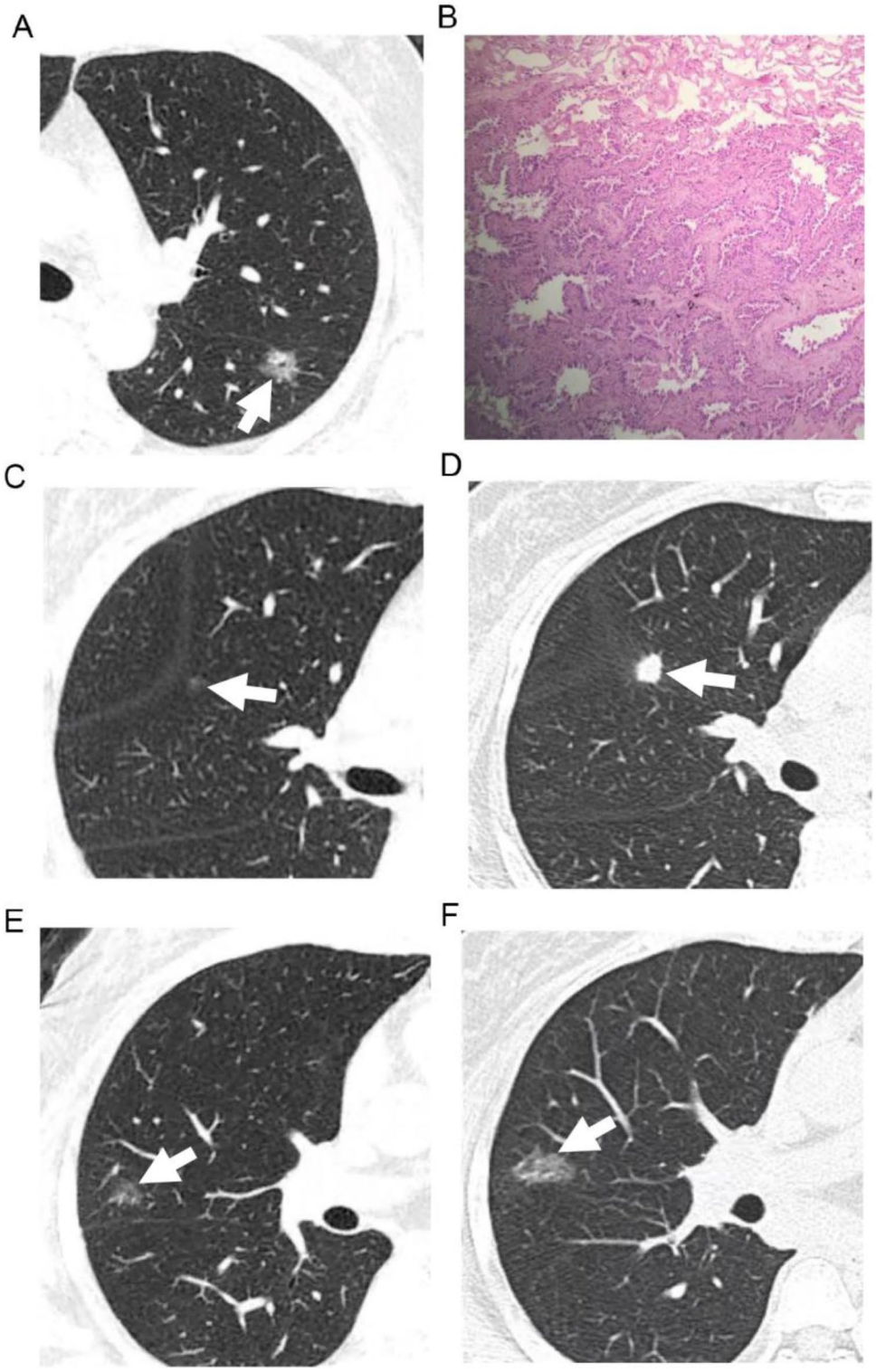

Fig. 4 Case study showing a 47-year-old female with multiple subsolid nodules. (**A**) The dominant tumor manifesting PSN (arrow) was located in the superior segment of the left lower lobe. (**B**) After segmentectomy, it was confirmed as an IAC with lepidic patterns (HE, ×40). (**C**) One RN in the right upper lobe was characterized as a pGGN (arrow) and measured 7.1 mm. (**D**) Postoperative imaging showed that the RN changed to a solid 9.0 mm nodule (arrow) after 5 years of follow-up. (**E**) Another RN (arrow) in the right middle lobe measured 6.2 mm. (**F**) This nodule (arrow) exhibited growth, reaching 15.6 mm, and developing a new solid component during 5 years of postoperative follow-up. Moreover, this patient developed right hilar lymph node metastasis during follow-up

Table 2 Characteristics of RNs in the growth and non-growth groups

Chracteristics	Total (603)	Growth group (108)	Non-growth group (495)	*P*
Lesion location				0.104
Left upper lobe	163 (27.0%)	36 (33.3%)	127 (25.7%)	
Left lower lobe	84 (14.0%)	11 (10.2%)	73 (14.8%)	
Right upper lobe	212 (35.2%)	29 (26.9%)	183 (37.0%)	
Right middle lobe	42 (7.0%)	9 (8.3%)	33 (6.7%)	
Right lower lobe	102 (16.9%)	23 (21.3%)	79 (16.0%)	
Morphological features				
Lesion size				0.000
< 5 mm	199 (33.0%)	8 (7.4%)	191 (38.6%)	
5–8 mm	239 (39.6%)	20 (18.5%)	219 (44.2%)	
≥ 8 mm	165 (27.4%)	80 (74.1%)	85 (17.2%)	
Nodular pattern				< 0.001
Pure GGN	568 (94.2%)	82 (75.9%)	486 (98.2%)	
PSN	35 (5.8%)	26 (24.1%)	9 (1.8%)	
Lobulated sign	20 (3.3%)	5 (4.6%)	15 (3.0%)	0.586
Spiculated sign	10 (1.7%)	7 (6.5%)	3 (0.6%)	< 0.001
Bronchial distortion	13 (2.2%)	9 (8.3%)	4 (0.8%)	< 0.001
Bubble lucency	26 (4.3%)	19 (17.6%)	7 (1.4%)	< 0.001
Vascular sign	565 (93.7%)	104 (96.3%)	461 (93.1%)	0.314
Pleural retraction	10 (1.7%)	5 (4.6%)	5 (1.0%)	0.024
Pleural attachment	77 (12.8%)	30 (27.8%)	47 (9.5%)	< 0.001
Well-defined margin	250 (41.5%)	37 (34.3%)	213 (43.0%)	0.117
Quantitative parameters				
3D maximum diameter (mm)	6.6 (5.2–7.7)	8.67 (7.5–12.5)	6.34 (5.0-7.1)	< 0.001
Mean CT value (HU)	-673 (-729.0–597.1)	-614.1 (-686.2–531.0)	-681.8 (-739.2–610.6)	< 0.001
Volume (mm3)	87.78 (46.0-160.6)	237.89 (146.0-555.2)	74.1 (42.8-122.1)	< 0.001
Mass (mg)	226.63 (14.6–55.0)	98.75 (55.0-215.2)	22.32 (13.4–41.3)	< 0.001

Table 3 Performance metrics of the radiomics, morphological, quantitative, and combined models

Models	Training set				Testing set			
	AUC	Sensitivity	Specificity	Accuracy	AUC	Sensitivity	Specificity	Accuracy
Morphology	0.868	0.774	0.826	0.817	0.834	0.833	0.802	0.810
Quantitative	0.873	0.810	0.829	0.825	0.862	0.792	0.778	0.781
Radiomics	0.996	1.000	0.966	0.972	0.892	0.833	0.877	0.867
Combined	0.967	0.905	0.901	0.902	0.887	0.833	0.815	0.819

size, and mean CT value) were selected in the training set using univariate and multivariate logistic regression analyses for the construction of the morphological and the quantitative model, respectively. Finally, a combined model was constructed through a two-stage feature selection process, incorporated 18 discriminative features (15 radiomics and 3 morphological features, excluding conventional quantitative features) selected via LASSO regression [Details see Additional file 1].

Model performance and comparison

The predictive ability of radiomics, morphological, quantitative, and combined models for 5-year RN growth was assessed using AUC, sensitivity, specificity, and accuracy, as detailed in Table 3 for both training and testing sets. In the training set, the AUC values for the morphological, quantitative, radiomics, and combined models were 0.868 (95% CI: 0.83–0.90), 0.873 (95% CI: 0.84–0.91), 0.996 (95% CI: 0.99-1.00), and 0.967 (95% CI: 0.95–0.98) with an accuracy of 81.7%, 82.5%, 97.2%, and 90.2%, respectively. In the test set, AUC values for the morphological, quantitative, radiomics, and combined models were 0.834 (95% CI: 0.76–0.91), 0.862 (95% CI: 0.79–0.93), 0.892 (95% CI: 0.83–0.95), and 0.887 (95% CI: 0.82–0.95) with an accuracy of 81.0%, 78.1%, 86.7%, and 81.9%, respectively.

The radiomics model achieved a significantly higher AUC value when compared to the morphological model ($P < 0.05$), and a superior AUC value compared to the quantitative model ($P = 0.251$). Moreover, the radiomics model exhibited a comparable AUC value to the combined model ($P = 0.728$). Additionally, the NRI showed

Table 4 DeLong test and NRI of four models in the training and testing set

Model	Training set			Testing set		
	P (AUC)	NRI	*P* (NRI)	*P* (AUC)	NRI	*P* (NRI)
Quantitative vs. Morphology	0.715	0.038	0.096	0.367	-0.066	0.085
Radiomics vs. Morphology	< 0.001	0.366	< 0.001	0.049	0.074	0.017
Combined vs. Morphology	< 0.001	0.206	< 0.001	0.111	0.012	0.425
Radiomics vs. Quantitative	< 0.001	0.328	< 0.001	0.251	0.140	0.005
Combined vs. Quantitative	< 0.001	0.168	< 0.001	0.368	0.079	0.160
Combined vs. Radiomics	< 0.001	-0.160	< 0.001	0.728	-0.062	0.180

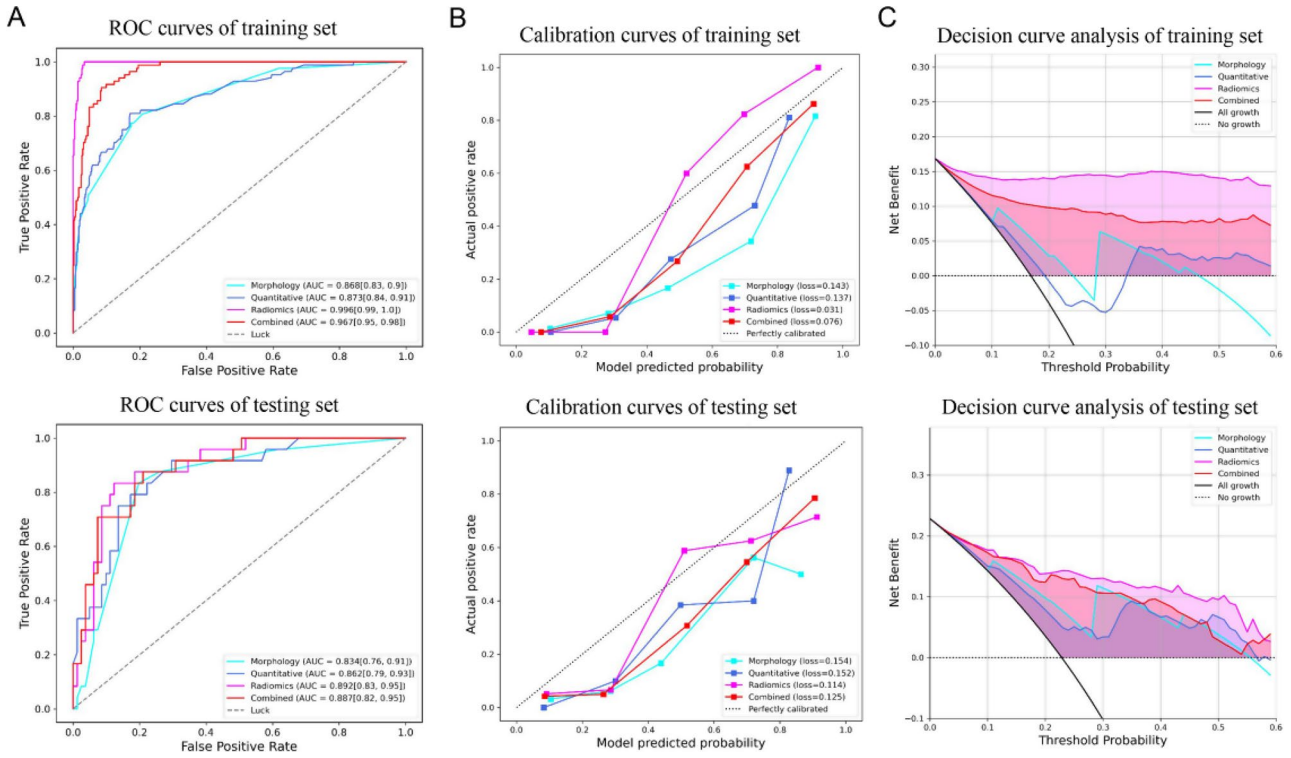

Fig. 5 ROC (**A**), calibration (**B**), and decision curves (**C**) of RN growth prediction

that the radiomics model was significantly superior to the morphological (NRI = 7.4%, $P = 0.017$) and quantitative (NRI = 14%, $P = 0.005$) models in terms of diagnostic performance (Table 4). Figure 5 illustrates the corresponding ROC, calibration, and decision curves.The assessment of four exhibited models utilized AUCs, calibration curves, and decision curves derived from the testing set. The calibration curves revealed that the radiomics model demonstrated enhanced predictive performance in the testing set, with a Brier loss of 0.114. The decision curve analyses illustrated that the radiomics model provided a higher net benefit compared to both the morphological and the quantitative models within a certain probability threshold range.

Discussion

This study established the prognostic superiority of preoperative CT radiomics in predicting 5-year growth of RNs, demonstrating both robust discriminative capacity (training/testing accuracy: 97.2%/86.7%) and optimal clinical utility. Notably, the radiomics model not only statistically outperformed traditional morphological and quantitative models but also achieved comparable performance to the combined model, suggesting its standalone sufficiency for clinical risk stratification. The superior performance of radiomics stems from its unique capacity to capture high-dimensional imaging heterogeneity, enabling more accurate identification of high-risk RNs for optimized surgical planning and postoperative surveillance. To our knowledge, this study pioneers utilizing radiomics to preoperatively predict the 5-year growth of RNs in patients who have undergone resection of their

dominant tumors, highlighting its promising potential for clinical guidance.

Morphological features observed on CT images are commonly utilized in clinical practice for differential diagnoses. In our study, a morphological model was developed based on 5 key features: size classification, nodular pattern, bronchial distortion, bubble lucency, and subpleural attachment. Our findings revealed that 48.5% of RNs with a lesion size ≥ 8 mm grew, while only 4.0% and 8.4% of RNs with a lesion size < 5 mm and between 5 and 8 mm grew, respectively. Lee et al. [26] reported that GGNs >8 mm in size tend to be malignant, and Cho et al. [14] demonstrated that this size range was an independent risk factor for subsequent GGNs growth, which was consistent with our study. The presence of a solid component in GGNs on CT images strongly correlates with the pathological invasive component. In our study, PSNs were identified as a key feature in the morphological model that influenced the growth of RN. This finding aligns with previous reports [14, 27]. Air bronchograms have been identified as independent risk factors for subsequent GGN growth [14]. The bronchus within GGNs may present as either natural or distorted [19]. Hence, we investigated signs of bronchial distortions, which were found to impact the 5-year growth of RNs. Similarly, bubble lucency has also been reported to be associated with GGN growth in a previous study [27]. However, pleural attachment emerged as a new morphological contributor to the growth of RNs. While morphological features have a prominent role in the clinic, their value may depend on the radiologist's experience and ability to identify specific signs. Additionally, most RNs were relatively small or subcentimeter nodules lacking morphological information, potentially contributing to the lower performance of the morphological model compared to the radiomics model in our study.

Quantitative parameters of CT imaging can identify the pathological invasiveness of GGNs [13, 28], and different quantitative parameters have been evaluated in various studies to predict GGN growth [25, 29–31]. Size was the most analyzed parameter and was mentioned in most morphological analyses [5, 14, 21]. For instance, Shi et al. [31] reported that a maximum diameter >10.2 mm was an independent predictor of pure GGN growth. Moreover, Qi et al. [29]showed that the initial volume was a determinant for GGN growth. Other studies [25, 30, 31] investigated quantitative parameters for GGN analysis using a more extensive set of features, such as CT attenuation values, standard deviations, CT number histograms, skewness, and linear mass densities. In our study, a quantitative model was constructed using the 3D maximum size and the mean CT value parameters. These parameters, although partially overlapping with radiomics features, represent distinct dimensions of imaging information and are widely used in clinical practice due to their interpretability. The results showed that the quantitative model (AUC: 0.862) performed well but was inferior to the radiomics model (AUC: 0.892), indicating that radiomics features provide additional valuable information.

Recently, radiomics has emerged as a robust method capable of converting medical images into quantitative descriptors of cancerous tissue. In our study, the selected radiomics features in the radiomics model reflect various tumor characteristics, encompassing 2 shape-related features, 14 texture-based features, and 2 first-order features, all of which hold potential clinical significance. The top-ranked feature, the original_shape_MajorAxisLength, is related to the size and shape of RNs, where a longer major Length may imply invasive growth, which is consistent with previous quantitative studies [5, 14, 21] and our clinical observations, where RNs larger than 8 mm show a significantly higher growth rate of 48.5%. In our study, features predominantly derived from the gray-level co-occurrence matrix, along with other texture-related parameters and first-order features, collectively delineate texture heterogeneity. Such heterogeneity, typically correlated with histopathological complexity, may signal malignant transformation, where clonal expansion, stromal remodeling, and vascular invasion generate spatially discordant patterns [32]. Previous studies [19, 22, 33] have proven the advantage of radiomics in the diagnosis of invasive GGNs compared to conventional radiographic features. Current predictive models [21, 34] have utilized radiomics to predict the growth of GGNs, often employing manual delineation for nodule segmentation in their studies. For instance, Sun et al. [21] developed a predictive nomogram (AUC = 0.843) combining radiomics and clinical features (size, location, and age) for the 5-year growth of GGNs, achieving similar AUC values to the radiomics model (AUC = 0.836). Gao et al. [34] developed a combined model to predict growth trends of GGNs with follow-up periods of at 2 years, reporting comparable discriminative performance between the combined model (AUC = 0.801) and radiomics-only approach (AUC = 0.803). Our model (radomics model, AUC = 0.892) outperforms previously reported results, indirectly demonstrating the superiority of employing a semi-automatic annotation strategy. In addition, our study further explores the construction of a 5-year growth prediction model for all RNs based on preoperative CT in patients undergoing resection of dominant tumors. This provides crucial guidance for clinical decision-making.

Feature selection for the combined model revealed important insights: LASSO regularization excluded all quantitative features due to multicollinearity with radiomic features, while preserving three clinically

significant morphological characteristics (vacuole sign, nodular pattern, pleural adhesion). Notably, the top-ranked radiomic biomarker, original_shape_MajorAxisLength, maintained its primary position in the combined model's feature set. This outcome suggests that while traditional quantitative features demonstrated multicollinearity with radiomic features and were consequently eliminated, certain clinician-assessed morphological characteristics retained independent predictive value. Particularly, features like pleural adhesion, which are challenging to capture through radiomic analysis alone, appear to provide complementary diagnostic information. Notably, the comparable performance between combined and radiomics models suggests that current feature integration approaches may not provide additional predictive value beyond radiomics analysis alone. This finding reinforces the superior capability of radiomics features in capturing essential tumor characteristics for growth prediction. Future studies may explore advanced deep learning architectures that may better synthesize these complementary data modalities.

In our study, the radiomics model not only outperformed the traditional models statistically, but also clinically, as evidenced by the decision curve analysis. While the morphological and quantitative models showed minimal or negative net benefits, especially at thresholds of around 0.2–0.3. These traditional models, while interpretable and easy to use, may lack the discriminatory power and consistency required for predicting growth. To enhance clinical relevance, our decision curve analysis employed a "All growth/Non-growth" framework (rather than the conventional "Treat all/none"). Here, the "growth" strategy involves making a choice between two mutually exclusive actions: synchronous surgical resection and intensified surveillance. "None growth" corresponds to standard guideline - based CT surveillance without immediate intervention. For the radiomics model, the sustained positive net benefit across a wide threshold probability range (0.1–0.6) indicates that it offers significant clinical benefits in identifying patients' definite progression risks and facilitating discussions on corresponding management strategies. That being said, when it comes to the selection of management strategies, it might be advisable to consider Threshold - Adaptive Strategies. For low thresholds, short - interval surveillance should be prioritized to relieve patient anxiety and prevent the failure to detect nodules that are growing at an early stage. In contrast, when making the decision to perform synchronous surgery, it is advisable to comprehensively consider multiple factors, including the location and traditional characteristics of RNs as well as the patient's psychological state.

This study has some limitations. First, the retrospective design introduces potential selection bias, though we mitigated this through multi-stage sampling and blinded radiomic feature extraction across consecutive surgical cases. Second, although our dual - reader approach enhanced the accuracy of RN identification, the study is still vulnerable to selection bias, particularly for small nodules or those obscured by anatomical structures. Third, our study was limited to a 5-year follow-up period. Its validity for ultra-long-term behavior requires verification through extended follow-up studies or serial radiomic assessments to evaluate temporal feature stability. Fourth, while our radiomic model demonstrated strong predictive value, their biological interpretability requires validation through multi-omics correlation studies. Prospective research combining deep radiomic phenotyping with genomic sequencing of RNs could elucidate how imaging features map to molecular progression mechanisms. However, the low resection rate of RNs may pose challenges for rapid acquisition of paired tissue samples, suggesting the need for innovative study designs such as liquid biopsy approaches or multicenter collaborations to overcome this limitation.

Conclusion

The radiomics model demonstrated superior performance in predicting 5-year growth of RNs, achieving high accuracy and robust discriminative ability compared to morphological and quantitative models. With excellent calibration and clinical utility, radiomics provides a reliable standalone tool for risk stratification, potentially optimizing postoperative surveillance strategies for patients with multiple lung subsolid nodules.

Abbreviations

GGNs	Ground-glass nodules
PSNs	Part-solid nodules
RNs	Residual nodules
PGL	Precursor glandular lesions
AAH	Atypical adenomatous hyperplasia
AIS	Adenocarcinoma in situ
MIA	Minimally invasive adenocarcinoma
IAC	Invasive adenocarcinoma
uRP	uAI Research Portal
LASSO	The least absolute shrinkage and selection operator regression
RF	Random Forest
NRI	Net reclassification improvement
ROC	The receiver operating characteristic
AUC	The area under the curve

Supplementary Information

The online version contains supplementary material available at https://doi.org/10.1186/s40644-025-00962-1.

Supplementary Material 1

Acknowledgements

We would like to thank Mengting Cai and Yuandi Zhuang, who provided assistance with the literature search and data collection.

Author contributions
G. Z. F. and S. M. M. designed the project; G. Z. F., E. H. X., G. Q. C., Y. Y. Y., X. W. Z., L. Y. L, J. J. L., J. H. C. and C. L. collected the data and assisted the data analysis; G. Z. F. and E. H. X. analyzed the data; G. Z. F. and S. M. M. wrote and revised the manuscript. All authors read and approved the final manuscript.

Funding
This study was supported by the Wenzhou Municipal Science and Technology Bureau Project, ZheJiang, China [grant number: Y2023196] and the Natural Science Foundation of Zhejiang Province, China [grant number: LTGY23H180010].

Data availability
No datasets were generated or analysed during the current study.

Declarations

Ethics approval and consent to participate
This study was approved by the Institutional Review and Ethical Committees of the first affiliated Hospital of Wenzhou Medical University (YS2023-No.493) and was conducted in accordance with the Declaration of Helsinki. Due to the retrospective nature of the study, the need for informed consent was waived.

Consent for publication
All authors have read and approved the manuscript and agree with submission to Cancer imaging.

Competing interests
The authors declare no competing interests.

Author details
[1]Depatment of Radiology, First Affiliated Hospital of Wenzhou Medical University, Wenzhou, Zhejiang 325000, China
[2]School of Public Health, Wenzhou Medical University, Wenzhou, Zhejiang 325000, China
[3]Department of Research and Development, United Imaging Intelligence, Shanghai 200232, China

Received: 20 April 2025 / Accepted: 17 November 2025
Published online: 29 December 2025

References

1. Siegel RL, Miller KD, Wagle NS, Jemal A. Cancer statistics, 2023. CA Cancer J Clin. 2023;73:17–48.
2. Aberle D, Adams A, Berg C, Black W, Clapp J, Fagerstrom R, Gareen I, Gatsonis C, Marcus P, Sicks J. Reduced lung-cancer mortality with low-dose computed tomographic screening. N Engl J Med. 2011;365:395–409.
3. Bonney A, Malouf R, Marchal C, Manners D, Fong KM, Marshall HM, Irving LB, Manser R. Impact of low-dose computed tomography (LDCT) screening on lung cancer-related mortality. Cochrane Database Syst Rev. 2022;8:Cd013829.
4. Sato Y, Fujimoto D, Morimoto T, Uehara K, Nagata K, Sakanoue I, Hamakawa H, Takahashi Y, Imai Y, Tomii K. Natural history and clinical characteristics of multiple pulmonary nodules with ground glass opacity. Respirology. 2017;22:1615–21.
5. Gao R, Berry M, Kunder C, Khuong A, Wakelee H, Neal J, Backhus L, Shrager J. Survival and risk factors for progression after resection of the dominant tumor in multifocal, lepidic-type pulmonary adenocarcinoma. J Thorac Cardiovasc Surg. 2017;154:2092–9. e2092.
6. Xia T, Cai M, Zhuang Y, Ji X, Huang D, Lin L, Liu J, Yang Y, Fu G. Risk factors for the growth of residual nodule in surgical patients with adenocarcinoma presenting as multifocal Ground-glass nodules. (1872–7727 (Electronic)).
7. Goldstraw P, Chansky K, Crowley J, Rami-Porta R, Asamura H, Eberhardt WE, Nicholson AG, Groome P, Mitchell A, Bolejack V. The IASLC lung cancer staging project: proposals for revision of the TNM stage groupings in the forthcoming (Eighth) edition of the TNM classification for lung cancer. J Thorac Oncology: Official Publication Int Association Study Lung Cancer. 2016;11:39–51.
8. MacMahon H, Naidich DP, Goo JM, Lee KS, Leung ANC, Mayo JR, Mehta AC, Ohno Y, Powell CA, Prokop M, et al. Guidelines for management of incidental pulmonary nodules detected on CT images: from the Fleischner society 2017. Radiology. 2017;284:228–43.
9. Kim HY, Shim YM, Lee KS, Han J, Yi CA, Kim YK. Persistent pulmonary nodular ground-glass opacity at thin-section CT: histopathologic comparisons. Radiology. 2007;245:267–75.
10. Barsky SH, Cameron R, Osann KE, Tomita D, Holmes EC. Rising incidence Ofbronchioloalveolar lung carcinoma and its unique clinicopathologic features. Cancer. 1994;73:1163–70.
11. Christensen J, Prosper AE, Wu CC, Chung J, Lee E, Elicker B, Hunsaker AR, Petranovic M, Sandler KL, Stiles B, et al. ACR Lung-RADS v2022: assessment categories and management recommendations. Chest. 2024;165:738–53.
12. Kakinuma R, Muramatsu Y, Kusumoto M, Tsuchida T, Tsuta K, Maeshima AM, Asamura H, Moriyama N. Solitary pure ground-glass nodules 5 mm or smaller: frequency of growth. Radiology. 2015;276:873–82.
13. Lim HJ, Ahn S, Lee KS, Han J, Shim YM, Woo S, Kim JH, Yie M, Lee HY, Yi CA. Persistent pure ground-glass opacity lung nodules ≥ 10 mm in diameter at CT scan: histopathologic comparisons and prognostic implications. Chest. 2013;144:1291–9.
14. Cho J, Kim E, Kim S, Lee Y, Park J, Cho Y, Yoon H, Lee J, Lee C. Long-Term Follow-up of small pulmonary Ground-Glass nodules stable for 3 years: implications of the proper Follow-up period and risk factors for subsequent growth. J Thorac Oncology: Official Publication Int Association Study Lung Cancer. 2016;11:1453–9.
15. Silva M, Prokop M, Jacobs C, Capretti G, Sverzellati N, Ciompi F, van Ginneken B, Schaefer-Prokop C, Galeone C, Marchianò A, et al. Long-Term active surveillance of screening detected subsolid nodules is a safe strategy to reduce overtreatment. J Thorac Oncology: Official Publication Int Association Study Lung Cancer. 2018;13:1454–63.
16. Lee JH, Lim WH, Hong JH, Nam JG, Hwang EJ, Kim H, Goo JM, Park CM. Growth and clinical impact of 6-mm or larger subsolid nodules after 5 years of stability at chest CT. Radiology. 2020:191921.
17. Lee K, Kim HR, Park SI, Kim DK, Kim YH, Choi S, Lee GD. Natural progression of Ground-glass nodules after curative resection for Non-small cell lung cancer. J Korean Med Sci. 2021;36:e266.
18. Lambin P, Leijenaar RTH, Deist TM, Peerlings J, de Jong EEC, van Timmeren J, Sanduleanu S, Larue R, Even AJG, Jochems A, et al. Radiomics: the Bridge between medical imaging and personalized medicine. Nat Reviews Clin Oncol. 2017;14:749–62.
19. Fan L, Fang M, Li Z, Tu W, Wang S, Chen W, Tian J, Dong D, Liu S. Radiomics signature: a biomarker for the preoperative discrimination of lung invasive adenocarcinoma manifesting as a ground-glass nodule. Eur Radiol. 2019;29:889–97.
20. Shi L, Zhao J, Peng X, Wang Y, Liu L, Sheng M. CT-based radiomics for differentiating invasive adenocarcinomas from indolent lung adenocarcinomas appearing as ground-glass nodules: asystematic review. Eur J Radiol. 2021;144:109956.
21. Sun Y, Ma Z, Zhao W, Jin L, Gao P, Wang K, Huang X, Duan S, Li M. Computed tomography radiomics in growth prediction of pulmonary ground-glass nodules. Eur J Radiol. 2023;159:110684.
22. Sun Y, Li C, Jin L, Gao P, Zhao W, Ma W, Tan M, Wu W, Duan S, Shan Y, et al. Radiomics for lung adenocarcinoma manifesting as pure ground-glass nodules: invasive prediction. Eur Radiol. 2020;30:3650–9.
23. Wu J, Xia Y, Wang X, Wei Y, Liu A, Innanje A, Zheng M, Chen L, Shi J, Wang L, et al. uRP: an integrated research platform for one-stop analysis of medical images. Front Radiol. 2023;3:1153784.
24. Zhao Q, Wang JW, Yang L, Xue LY, Lu WW. CT diagnosis of pleural and stromal invasion in malignant subpleural pure ground-glass nodules: an exploratory study. Eur Radiol. 2019;29:279–86.
25. Bak SH, Lee HY, Kim JH, Um SW, Kwon OJ, Han J, Kim HK, Kim J, Lee KS. Quantitative CT scanning analysis of pure Ground-Glass opacity nodules predicts further CT scanning change. Chest. 2016;149(1):180–91.
26. Lee HJ, Goo JM, Lee CH, Park CM, Kim KG, Park EA, Lee HY. Predictive CT findings of malignancy in ground-glass nodules on thin-section chest CT: the effects on radiologist performance. Eur Radiol. 2009;19:552–60.
27. Kakinuma R, Noguchi M, Ashizawa K, Kuriyama K, Maeshima A, Koizumi N, Kondo T, Matsuguma H, Nitta N, Ohmatsu H, et al. Natural history of pulmonary subsolid nodules: A prospective multicenter study. J Thorac Oncology: Official Publication Int Association Study Lung Cancer. 2016;11:1012–28.
28. Godoy MC, Naidich DP. Subsolid pulmonary nodules and the spectrum of peripheral adenocarcinomas of the lung: recommended interim guidelines for assessment and management. Radiology. 2009;253:606–22.

29. Qi LL, Wang JW, Yang L, Huang Y, Zhao SJ, Tang W, Jin YJ, Zhang ZW, Zhou Z, Yu YZ, et al. Natural history of pathologically confirmed pulmonary subsolid nodules with deep learning-assisted nodule segmentation. Eur Radiol. 2021;31:3884–97.
30. Borghesi A, Coviello F, Scrimieri A, Ciolli P, Ravanelli M, Farina D. Software-based quantitative CT analysis to predict the growth trend of persistent non-solid pulmonary nodules: a retrospective study. Radiol Med. 2023;128:734–43.
31. Shi Z, Deng J, She Y, Zhang L, Ren Y, Sun W, Su H, Dai C, Jiang G, Sun X, et al. Quantitative features can predict further growth of persistent pure ground-glass nodule. Quant Imaging Med Surg. 2019;9:283–91.
32. Ren YF, Ma Q, Zeng X, Huang CX, Ren JL, Li F, Tong JJ, He JW, Zhong Y, Tan SY, et al. Single-cell RNA sequencing reveals immune microenvironment niche transitions during the invasive and metastatic processes of ground-glass nodules and part-solid nodules in lung adenocarcinoma. Mol Cancer. 2024;23:263.
33. Nishino M. Radiomics to predict invasiveness of Part-Solid adenocarcinoma of the lung. Radiology. 2020;297:459–61.
34. Gao C, Yan J, Luo Y, Wu L, Pang P, Xiang P, Xu M. The growth trend predictions in pulmonary ground glass nodules based on radiomic CT features. Front Oncol. 2020;10:580809.

Publisher's note